

# Gravitational softening as a smoothing operation

Joshua E. Barnes

*Institute of Astronomy, University of Hawaii, 2680 Woodlawn Drive, Honolulu, HI 96822, USA*

24 August 2012

## ABSTRACT

In self-consistent  $N$ -body simulations of collisionless systems, gravitational interactions are modified on small scales to remove singularities and simplify the task of numerically integrating the equations of motion. This ‘gravitational softening’ is sometimes presented as an ad-hoc departure from Newtonian gravity. However, softening can also be described as a smoothing operation applied to the mass distribution; the gravitational potential and the smoothed density obey Poisson’s equation precisely. While ‘softening’ and ‘smoothing’ are mathematically equivalent descriptions, the latter has some advantages. For example, the smoothing description suggests a way to set up  $N$ -body initial conditions in almost perfect dynamical equilibrium.

**Key words:** methods: numerical – galaxies: kinematics & dynamics

## 1 INTRODUCTION

The evolution of a collisionless self-gravitating system is described by two coupled equations: the Vlasov equation,

$$\frac{\partial f}{\partial t} + \mathbf{v} \cdot \frac{\partial f}{\partial \mathbf{r}} - \nabla \Phi \cdot \frac{\partial f}{\partial \mathbf{v}} = 0, \quad (1)$$

where  $f = f(\mathbf{r}, \mathbf{v}, t)$  is the one-particle distribution function and  $\Phi(\mathbf{r}, t)$  is the gravitational potential, and Poisson’s equation,

$$\nabla^2 \Phi = 4\pi G \rho = 4\pi G \int d\mathbf{v} f. \quad (2)$$

$N$ -body simulations use a Monte-Carlo method to solve these equations. The distribution function is represented by a collection of  $N$  particles (Klimontovich 1967):

$$f(\mathbf{r}, \mathbf{v}, t) = \sum_{i=1}^N m_i \delta^3(\mathbf{r} - \mathbf{r}_i(t)) \delta^3(\mathbf{v} - \mathbf{v}_i(t)), \quad (3)$$

where  $m_i$ ,  $\mathbf{r}_i$ , and  $\mathbf{v}_i$  are the mass, position, and velocity of particle  $i$ . Over time, particles move along characteristics of (1); at each instant, their positions provide the density needed for (2).

In many collisionless  $N$ -body simulations, the equations of motion actually integrated are

$$\frac{d\mathbf{r}_i}{dt} = \mathbf{v}_i, \quad \frac{d\mathbf{v}_i}{dt} = \sum_{j \neq i}^N G m_j \frac{\mathbf{r}_j - \mathbf{r}_i}{(|\mathbf{r}_j - \mathbf{r}_i|^2 + \epsilon^2)^{3/2}}, \quad (4)$$

where  $\epsilon$  is the *softening length*. These equations reduce to the standard Newtonian equations of motion if  $\epsilon = 0$ . The main reason for setting  $\epsilon \neq 0$  is to suppress the  $1/r$  singularity in the Newtonian potential; this greatly simplifies the task of numerically integrating these equations (e.g., Dehnen 2001). By limiting the spatial resolution of the gravitational force, softening also helps control fluctuations caused by sampling the distribution function with finite  $N$ ; however, this comes at a price, since the gravitational field is systematically biased for  $\epsilon \neq 0$  (Merritt 1996; Athanassoula et al. 1998, 2000).

Softening is often described as a modification of Newtonian gravity, with the  $1/r$  potential replaced by  $1/\sqrt{r^2 + \epsilon^2}$ . The latter is proportional to the potential of a Plummer (1911) sphere with scale radius  $\epsilon$ . This does *not* imply that particles interact like Plummer spheres (Dyer & Ip 1993); the acceleration of particle  $i$  is computed from the field at the point  $\mathbf{r}_i$  only. But it does imply that softening can also be described as a smoothing operation (e.g., Hernquist & Barnes 1990), in which the pointillistic Monte-Carlo representation of the density field is convolved with the kernel

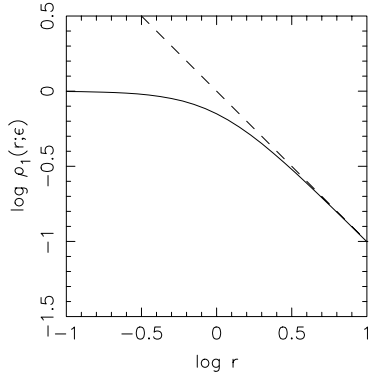


**Figure 1.** Effect of Plummer smoothing on a  $\rho \propto r^{-1}$  profile. Dashed line is the underlying density profile; solid curve is the result of smoothing with  $\epsilon = 1$ . The smoothed profile is always less than the underlying power-law.

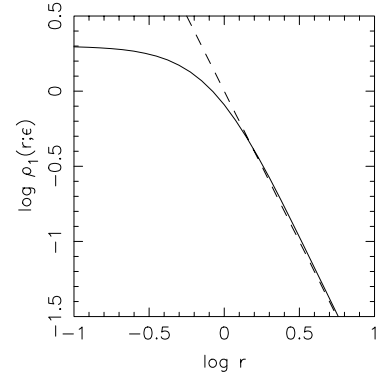


**Figure 2.** Effect of Plummer smoothing on a  $\rho \propto r^{-2}$  profile. Dashed line is the underlying density profile; solid curve is the result of smoothing with  $\epsilon = 1$ . The smoothed profile slightly exceeds the underlying power-law at large  $r$ .

$$S(r; \epsilon) = \frac{3}{4\pi} \frac{\epsilon^2}{(r^2 + \epsilon^2)^{5/2}}. \quad (5)$$

In effect, the source term for Poisson's equation (2) is replaced with the *smoothed density*

$$\rho(\mathbf{r}; \epsilon) \equiv \int d\mathbf{r}' \rho(\mathbf{r}') S(|\mathbf{r} - \mathbf{r}'|; \epsilon) = \int d\mathbf{r}' \rho(\mathbf{r} - \mathbf{r}') S(|\mathbf{r}'|; \epsilon). \quad (6)$$

Formally, (4) provides a Monte-Carlo solution to the Vlasov equation (1) coupled with

$$\nabla^2 \Phi = 4\pi G \rho(\mathbf{r}; \epsilon) = 4\pi G \int d\mathbf{r}' \int d\mathbf{v} f(\mathbf{r}', \mathbf{v}, t) S(|\mathbf{r} - \mathbf{r}'|; \epsilon). \quad (7)$$

Thus one may argue that a softened  $N$ -body simulation actually uses standard Newtonian gravity, as long as it is clear that the mass distribution generating the gravitational field is derived from the particles via a smoothing process.

Although Plummer softening is widely used in  $N$ -body simulations, its effects are incompletely understood. If the underlying density field is featureless on scales of order  $\epsilon$ , softening has relatively little effect. However,  $N$ -body simulations are often used to model systems with power-law density profiles; for example, Hernquist (1990) and Navarro, Frenk, & White (1996, hereafter NFW) models, which have  $\rho \propto r^{-1}$  at small  $r$ , are widely used as initial conditions. One purpose of this paper is to examine how softening modifies such profiles.

Assume that the underlying density profile is spherically symmetric and centered on the origin:  $\rho = \rho(|\mathbf{r}|)$ . The integrand in (6) is unchanged by rotation about the axis containing the origin and the point  $\mathbf{r}$ , so the integral can be simplified by adopting cylindrical coordinates  $(\varphi, R, z)$ , where  $\mathbf{r}$  is located on the  $z$ -axis at  $z = |\mathbf{r}|$ . The integral over  $\varphi$  is trivial; for Plummer smoothing, the result is

$$\rho(r; \epsilon) = \frac{3\epsilon^2}{2} \int_{-\infty}^{\infty} dz \int_0^{\infty} dR R \frac{\rho(\sqrt{R^2 + z^2})}{(R^2 + (z - r)^2 + \epsilon^2)^{5/2}} = \frac{3\epsilon^2}{2} \int_{-\infty}^{\infty} dz \int_0^{\infty} dR R \frac{\rho(\sqrt{R^2 + (z - r)^2})}{(R^2 + z^2 + \epsilon^2)^{5/2}}, \quad (8)$$

where the second equality holds because the outer integral is taken over the entire  $z$  axis.

## 2 POWER-LAW PROFILES

The first step is to examine the effect of Plummer smoothing on power-law density profiles,  $\rho_n(r) = \rho_a(a/r)^n$ , where  $0 < n < 3$ . These profiles are not realistic, since the total mass diverges as  $r \rightarrow \infty$ . However, results obtained for power-law profiles help interpret the effects of smoothing on more realistic models.

### 2.1 The case $\rho \propto r^{-1}$

Let the density be  $\rho_1(r) = \rho_a(a/r)$ . The total mass enclosed within radius  $r$  is  $M_1(r) = 2\pi\rho_a ar^2$ . In this case, the smoothed density profile can be calculated analytically; the double integral is

$$\int_{-\infty}^{\infty} dz \int_0^{\infty} dR R \frac{(R^2 + (z - r)^2)^{-1/2}}{(R^2 + z^2 + \epsilon^2)^{5/2}} = \frac{2}{3\epsilon^2 \sqrt{\epsilon^2 + r^2}}. \quad (9)$$

This yields a remarkably simple result for the smoothed density, plotted in Fig. 1,

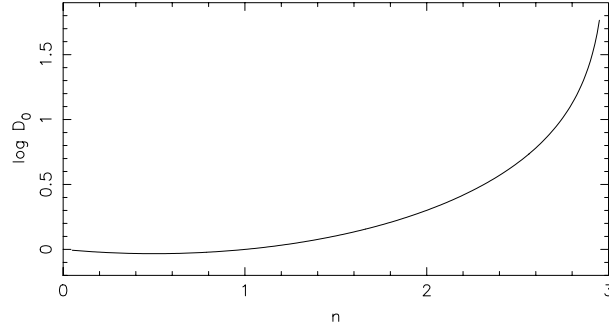


**Figure 3.** Density ratio  $D_0 = \rho_n(0; \epsilon) / \rho_n(\epsilon)$  plotted as a function of  $n$ . Limiting values are  $D_0 = 1$  as  $n \rightarrow 0$  and  $D_0 = \infty$  as  $n \rightarrow 3$ .

$$\rho_1(r; \epsilon) = \rho_a \frac{a}{\sqrt{\epsilon^2 + r^2}} = \rho_1(\sqrt{\epsilon^2 + r^2}) = \rho_1(r_\epsilon), \quad (10)$$

where  $r_\epsilon \equiv \sqrt{\epsilon^2 + r^2}$ . The smoothed mass within radius  $r$ , hereafter called the *smoothed mass profile*<sup>1</sup>, is

$$M_1(r; \epsilon) = \int_0^r dx 4\pi x^2 \rho_1(x; \epsilon) = 2\pi \rho_a a (rr_\epsilon - \epsilon^2 \sinh^{-1}(r/\epsilon)). \quad (11)$$

## 2.2 The case $\rho \propto r^{-2}$

Let the density be  $\rho_2(r) = \rho_a(a/r)^2$ . The total mass enclosed within radius  $r$  is  $M_2(r) = 4\pi \rho_a a^2 r$ . The integral over  $R$  can be evaluated, but the result is not particularly informative and the remaining integral must be done numerically. Fig. 2 presents the results. For  $\log(r) \gtrsim 0.2$ , the smoothed density exceeds the underlying power-law profile. This occurs because smoothing, in effect, spreads mass from  $r \lesssim \epsilon$  to larger radii, and with the underlying profile dropping away so steeply this redistributed mass makes a relatively large contribution to  $\rho_2(r; \epsilon)$ . Note that as  $r \rightarrow 0$ , the smoothed density  $\rho_2(r; \epsilon) \rightarrow 2\rho_2(\epsilon)$ .

## 2.3 Central density

It appears impossible to calculate the smoothed density profile for arbitrary  $n$  without resorting to numerical methods, but the central density is another matter. Setting  $r = 0$ , the smoothed density is

$$\rho_n(0; \epsilon) = 3\epsilon^2 \int_0^\infty dx \frac{x^2 \rho_n(x)}{(x^2 + \epsilon^2)^{5/2}} = \frac{n}{\sqrt{\pi}} \Gamma(\frac{3}{2} - \frac{n}{2}) \Gamma(\frac{n}{2}) \rho_n(\epsilon). \quad (12)$$

The central density ratio  $D_0(n) = \rho_n(0; \epsilon) / \rho_n(\epsilon)$  is plotted as a function of  $n$  in Fig. 3. For  $n = 1$  and  $2$ , the ratio  $D_0 = 1$  and  $2$ , respectively, in accord with the results above, while as  $n \rightarrow 3$  the central density diverges.

The smoothed central density for an arbitrary power-law is useful in devising an approximate expression for the smoothed density profile (Appendix A.1). In addition, the central density is related to the shortest dynamical time-scale present in an  $N$ -body simulation, which may in turn be used to estimate a maximum permissible value for the time-step (§ 4.3.1).

## 3 ASTROPHYSICAL MODELS

### 3.1 Hernquist and NFW models

As noted above, both of these profiles have  $\rho \propto r^{-1}$  as  $r \rightarrow 0$ . For this reason, they are treated in parallel. The Hernquist (1990) model has density and mass profiles

$$\rho_H(r) = \frac{aM}{2\pi r(a+r)^3}, \quad M_H(r) = \frac{Mr^2}{(r+a)^2}, \quad (13)$$

where  $a$  is the scale radius and  $M$  is the total mass. The Navarro, Frenk, & White (1996) model has density and mass profiles

$$\rho_{\text{NFW}}(r) = \frac{a^3 \rho_0}{r(a+r)^2}, \quad M_{\text{NFW}}(r) = 4\pi \rho_0 a^3 \left( \log \left( \frac{a+r}{a} \right) - \frac{r}{a+r} \right), \quad (14)$$

where  $a$  is again the scale radius and  $\rho_0$  is a characteristic density. The double integrals required to evaluate the smoothed versions of these profiles appear intractable analytically<sup>2</sup> but can readily be calculated numerically. Figs. 4 and 5 present

<sup>1</sup> This profile can't be obtained by applying kernel smoothing directly to  $M(r)$ ; only density profiles can be smoothed.

<sup>2</sup> Smoothed *central* densities for these and other profiles can be expressed in terms of special functions.

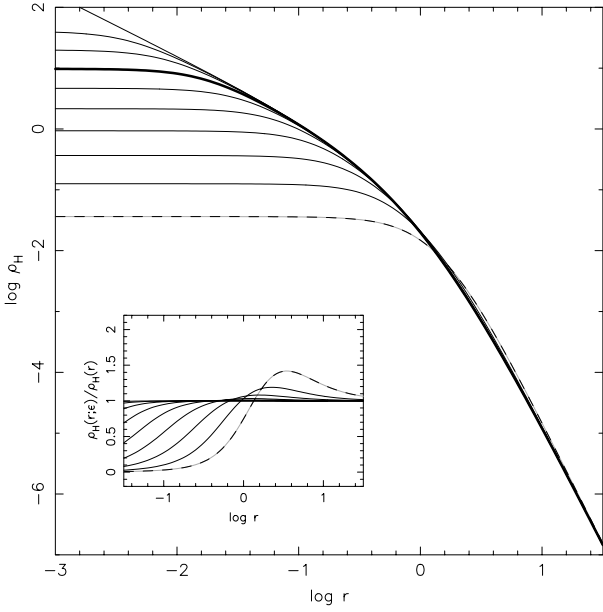


**Figure 4.** Effect of Plummer smoothing on Hernquist profile. Top curve shows the density profile of a Hernquist model with scale radius  $a = 1$  and mass  $M = 1$ . Lower curves show profiles smoothed with  $\epsilon = 1/256, 1/128, \dots, 1$  (from top to bottom); heavy curve is  $\epsilon = 1/64$ , dashed curve is  $\epsilon = 1$ . Inset shows ratio  $\rho_H(r; \epsilon)/\rho_H(r)$ .

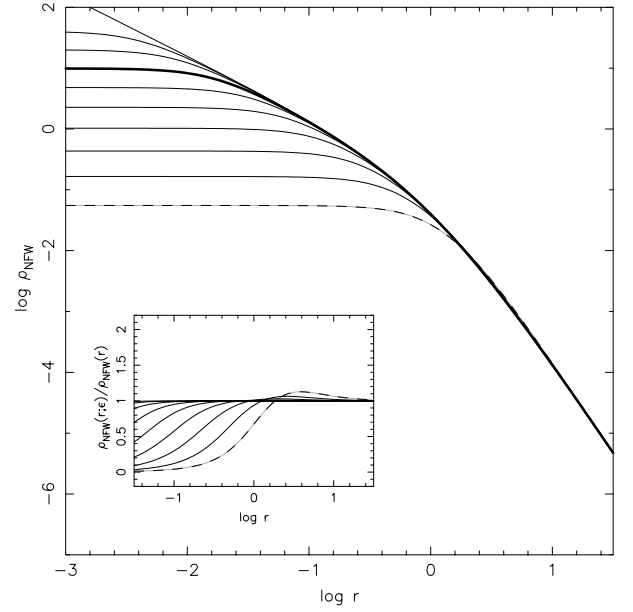


**Figure 5.** Effect of Plummer smoothing on NFW profile. Top curve shows the density profile of a NFW model with scale radius  $a = 1$  and density  $\rho_0 = 1/(2\pi)$ . Lower curves show profiles smoothed with  $\epsilon = 1/256, 1/128, \dots, 1$  (from top to bottom); heavy curve is  $\epsilon = 1/64$ , dashed curve is  $\epsilon = 1$ . Inset shows ratio  $\rho_{\text{NFW}}(r; \epsilon)/\rho_{\text{NFW}}(r)$ .

results for a range of  $\epsilon$  values between  $a$  and  $a/256$ . For comparison, both models are scaled to have the same underlying density profile at  $r \ll a$ .

The smoothed profiles shown in Figs. 4 and 5 are, for the most part, easily understood in terms of the results obtained for power-laws. For radii  $r < \epsilon$ , smoothing transforms central cusps into constant-density cores, just as in Fig. 1. If the softening length  $\epsilon$  is much less than the scale length  $a$ , the smoothed density  $\rho(r; \epsilon)$  within  $r \ll a$  is almost independent of the underlying profile at radii  $r > a$ . Consequently, the smoothed central density  $\rho(0; \epsilon) \simeq \rho(\epsilon)$ , echoing the result obtained for the power-law  $n = 1$ . In addition, the actual curves in Figs. 4 and 5 are shifted versions of the curves in Fig. 1; this observation motivates simple approximations to  $\rho_H(r; \epsilon)$  and  $\rho_{\text{NFW}}(r; \epsilon)$  described in Appendix A.2.

On the other hand, if  $\epsilon$  is comparable to  $a$ , the quantitative agreement between these profiles and the smoothed  $n = 1$  profile breaks down; the smoothed density at small  $r$  has a non-negligible contribution from the underlying profile beyond the scale radius  $a$ . As an example, for  $\epsilon = 1$  the central density of the smoothed NFW profile is higher than the central density of the smoothed Hernquist profile, because the former receives a larger contribution from mass beyond the scale radius.

A somewhat more subtle result, shown in the insets, is that heavily smoothed profiles *exceed* the underlying profiles at radii  $r \gtrsim a$ . This is basically the same effect found with the  $n = 2$  power-law profile (§ 2.2); with the underlying density dropping rapidly as a function of  $r$ , the mass spread outward from smaller radii more than makes up for the mass spread to still larger radii. This effect is more evident for the Hernquist profile than for the NFW profile because the former falls off more steeply for  $r \gtrsim a$ .

### 3.2 Jaffe model

The Jaffe (1983) model has density and mass profiles

$$\rho_J(r) = \frac{aM}{4\pi r^2(a+r)^2}, \quad M_J(r) = \frac{Mr}{(r+a)}, \quad (15)$$

where  $a$  is the scale radius and  $M$  is the total mass. The double integrals required to evaluate the smoothed version of this profile appear intractable analytically but can readily be calculated numerically. Fig. 6 present results for a range of  $\epsilon$  values between  $a$  and  $a/256$ .

Again, much of the behavior shown in this plot can be understood by reference to the results for the  $n = 2$  power-law. In particular, for smoothing lengths  $\epsilon \ll a$ , the central density is  $\rho_J(0; \epsilon) \simeq 2\rho_J(\epsilon)$ , and the curves in Fig. 6 are shifted versions of the one in Fig. 2. As the inset shows, for larger values of  $\epsilon$  the smoothed profiles quite noticeably exceed the underlying profile; the effect is stronger here than it is for a Hernquist model because the Jaffe model has more mass within  $r \leq a$  to redistribute.

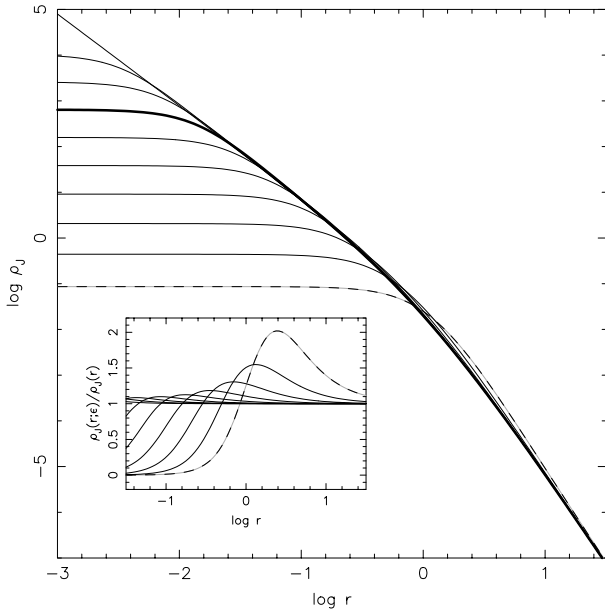


**Figure 6.** Effect of Plummer smoothing on Jaffe profile. Top curve shows the density profile of a Jaffe model with scale radius  $a = 1$  and mass  $M = 1$ . Lower curves show profiles smoothed with  $\epsilon = 1/256, 1/128, \dots, 1$  (from top to bottom); heavy curve is  $\epsilon = 1/64$ , dashed curve is  $\epsilon = 1$ . Inset shows ratio  $\rho_J(r; \epsilon)/\rho_J(r)$ .

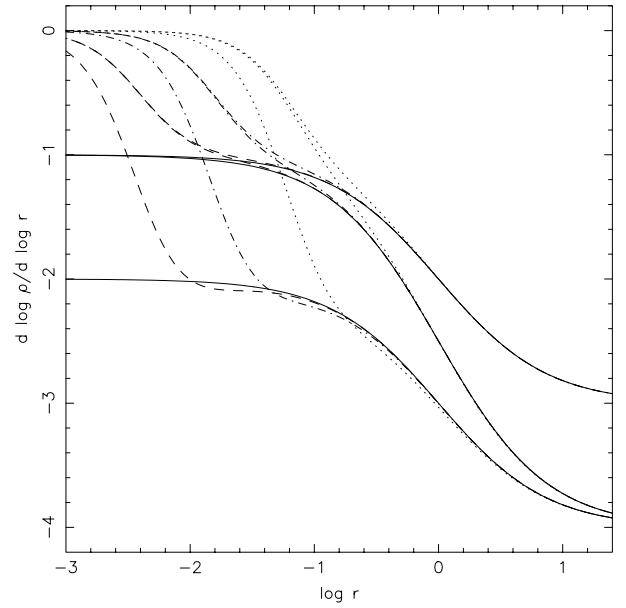


**Figure 7.** Logarithmic slopes of profiles from Figs. 4, 5, and 6. Solid lines are underlying profiles; from bottom to top, they represent Jaffe, Hernquist, and NFW models, respectively. Dashed, dot-dashed, and dotted lines give results for  $\epsilon = a/256, a/64$ , and  $a/16$ , respectively.

### 3.3 How much softening is too much?

Figs. 4, 5, and 6 have interesting implications for  $N$ -body experiments. One might expect the smoothed profiles to resolve the inner power-laws of the underlying models as long as the softening length  $\epsilon$  is somewhat less than the scale radius  $a$ , but that is not what these figures show. Profiles smoothed with  $\epsilon \gtrsim a/16$  are essentially constant-density cores attached to power-law outer profiles; the density within the core depends on  $\epsilon$ , but no inner cusp per se can be seen. For  $\epsilon \lesssim a/64$ , on the other hand, the smoothed profiles do appear to trace the inner power-laws over some finite range of radii, before flattening out at smaller  $r$ . Only for  $\epsilon \lesssim a/256$  can the inner cusps be followed for at least a decade in radius.

Fig. 7 helps explain this result. The underlying Jaffe, Hernquist, and NFW profiles all roll over gradually from their inner to outer power-law slopes between radii  $0.1a \lesssim r \lesssim 10a$ . Thus a resolution somewhat better than  $0.1a$  is required to see the inner cusps of these models. In practice, this implies the softening parameter  $\epsilon$  must be several times smaller than  $0.1a$ .

## 4 TESTS AND APPLICATIONS

Since the formalism developed above is exact, numerical tests of a relation like (8) for the smoothed density  $\rho(r; \epsilon)$  may seem superfluous. In practice, such tests can be illuminating – as benchmarks of  $N$ -body technique. In what follows, the smoothing formalism will be applied to actual  $N$ -body calculations, to check  $N$ -body methodology and to demonstrate that the formalism has real applications.

Putting this plan into operation requires some care. To begin with, an  $N$ -body realization of a standard Hernquist or Jaffe profile spans a huge range of radii. Typically, the innermost particle has radius  $r_{\text{in}} \sim aN^{-1/2}$  or  $aN^{-1}$  for a Hernquist or Jaffe profile, respectively, while for either profile, the outermost particle has radius  $r_{\text{out}} \sim aN$ . A dynamic range of  $r_{\text{out}}/r_{\text{in}} \sim N^{3/2}$  or  $N^2$  can be awkward to handle numerically; even gridless tree codes may not accommodate such enormous ranges gracefully. One simple option is to truncate the particle distribution at some fairly large radius, but it's preferable to smoothly taper the density profile:

$$\rho(r) \rightarrow \rho_t(r) = \begin{cases} (1 + \mu) \rho(r), & r \leq b \\ (1 + \mu) \rho_* (b/r)^2 e^{-r/r_*}, & r > b \end{cases} \quad (16)$$

where the taper radius  $b \gg a$ , the values of  $r_*$  and  $\rho_*$  are fixed by requiring that  $\rho_t(r)$  and its first derivative are continuous at  $r = b$ , and the value of  $\mu \ll 1$  is chosen to preserve the total mass. Let

$$\beta = \left. \frac{r}{\rho} \frac{d\rho}{dr} \right|_{r=b} \quad (17)$$

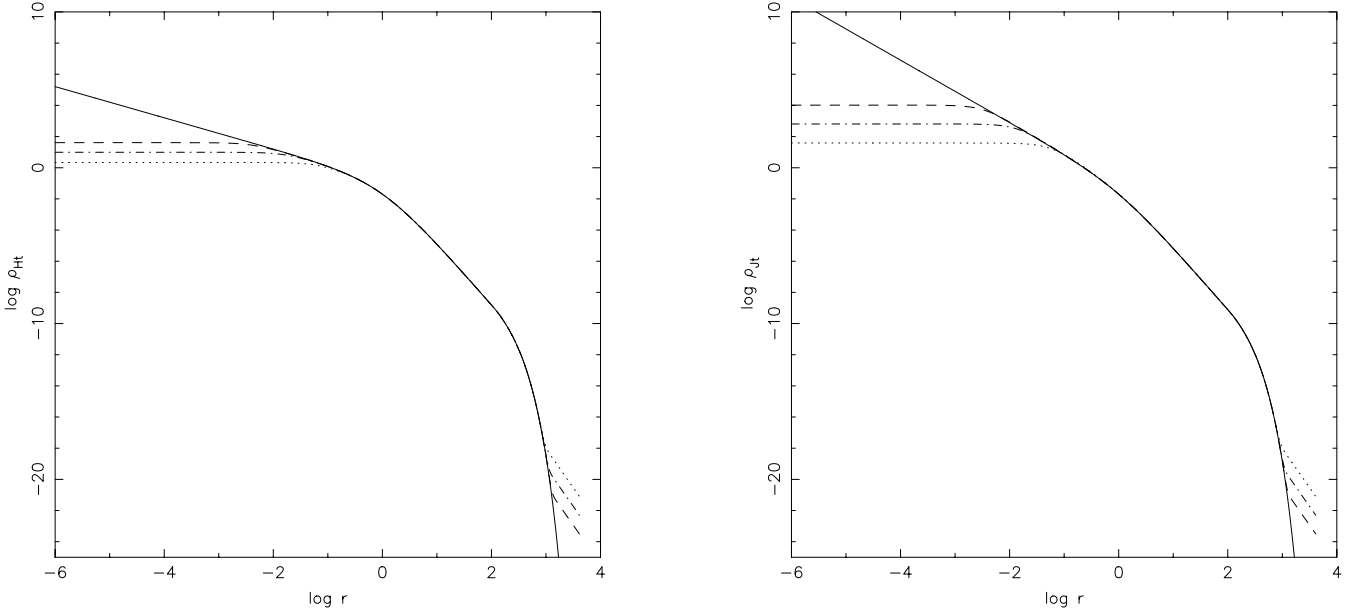


**Figure 8.** Effect of Plummer smoothing on tapered Hernquist (left) and Jaffe (right) models, represented by the solid curves. Dashed, dot-dashed, and dotted curves show results for  $\epsilon = 1/256$ ,  $1/64$ , and  $1/16$ , respectively.

be the logarithmic slope of the density profile at  $r = b$ , and  $M(r)$  be the underlying mass profile; then

$$r_* = \frac{b}{-(2+\beta)}, \quad \rho_* = \rho(b)e^{-(2+\beta)}, \quad \text{and} \quad \mu = \frac{M(\infty)}{M(b) + 4\pi b^2 r_* \rho(b)} - 1. \quad (18)$$

Fig. 8 shows how Plummer smoothing modifies tapered Hernquist and Jaffe profiles. Both profiles have scale radius  $a = 1$ , taper radius  $b = 100$ , and mass  $M = 1$ ; these parameters will be used in all subsequent calculations. In each case, the underlying profile follows the standard curve out to the taper radius  $b$ , and then rapidly falls away from the outer power law. At radii  $r \leq b$ , the smoothed profiles match those shown in Figs. 4 and 6, apart from the factor of  $(1 + \mu)$  used to preserve total mass. At larger radii, the smoothed profiles initially track the underlying tapered profiles, but then transition to asymptotic  $\rho \propto r^{-5}$  power law tails. This occurs because the Plummer smoothing kernel (5) falls off as  $r^{-5}$  at large  $r$ ; in fact, these power laws match  $\rho = 3M\epsilon^2/4\pi r^5$ , which is the large- $r$  approximation for a point mass  $M$  smoothed with a Plummer kernel. The amount of mass in these  $r^{-5}$  tails is negligible.

#### 4.1 Gravitational potentials

In principle, it's straightforward to verify that the smoothed profiles above generate potentials matching those obtained from  $N$ -body calculations. For a given density profile  $\rho(r)$ , construct a realization with  $N$  particles at positions  $\mathbf{r}_i$ ; a  $N$ -body force calculation with softening  $\epsilon$  yields the gravitational potential  $\Phi_i$  for each particle. Conversely, given the smoothed density profile  $\rho(r; \epsilon)$ , compute the smoothed mass profile  $M(r; \epsilon)$ , and use the result to obtain the *smoothed potential*  $\Phi(r; \epsilon)$ :

$$\frac{d\Phi}{dr} = G \frac{M(r; \epsilon)}{r^2}, \quad (19)$$

with boundary condition  $\Phi \rightarrow 0$  as  $r \rightarrow \infty$ . For each particle, the  $N$ -body potential  $\Phi_i$  may be compared with the predicted value  $\Phi(|\mathbf{r}_i|; \epsilon)$ ; apart from  $\sqrt{N}$  fluctuations, the two should agree.

A major complication is that  $\sqrt{N}$  fluctuations in  $N$ -body realizations imprint spatially coherent perturbations on the gravitational field; potentials measured at adjacent positions are not statistically independent. For example, the softened potential at the origin of an  $N$ -body system is

$$\Phi_0 = \sum_i \frac{Gm_i}{(r_i^2 + \epsilon^2)^{1/2}}. \quad (20)$$

If the radii  $r_i$  are independently chosen, this expression is a Monte Carlo integral, which will deviate from  $\Phi(0; \epsilon)$  by an amount of order  $O(N^{-1/2})$ ; moreover, everywhere within  $r \lesssim \epsilon$  the potential will deviate upward or downward by roughly as much as it does at  $r = 0$ . One way around this is to average over many  $N$ -body realizations, but this is tedious and expensive. An easier solution is to sample the radial distribution uniformly. Let  $M(r)$  be the mass profile associated with the underlying density  $\rho(r)$ . Assign all particles equal masses, and determine the radius  $r_i$  of particle  $i$  by solving  $M(r_i) = (i - 0.5)M(\infty)/N$  for

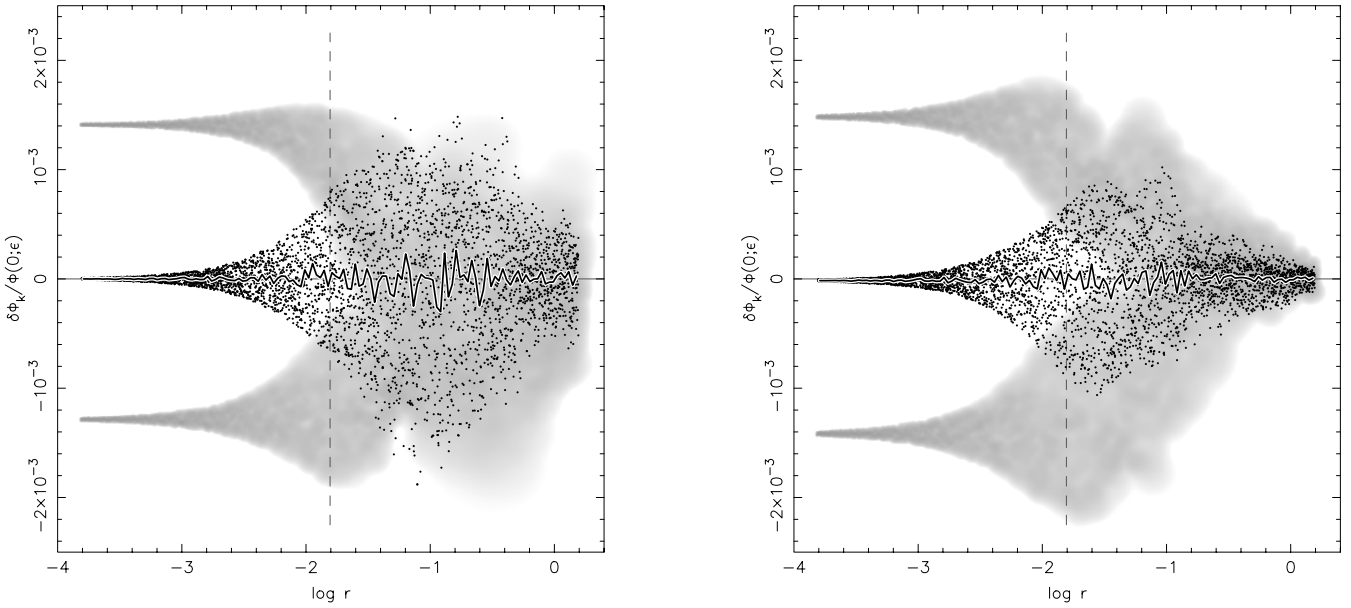


**Figure 9.** Difference  $\delta\Phi_k$  between  $N$ -body and smoothed potentials for tapered Hernquist (left) and Jaffe (right) models, normalized by central potential  $\Phi(0; \epsilon)$ . Vertical dashed lines show value of  $\epsilon = 1/64$ . Points are results for uniform realizations; jagged curves shows averages for groups of 32 points. Grey-scale images show typical results for *random* realizations. Central potentials are  $\Phi_H(0; \epsilon) = -0.9809$  and  $\Phi_J(0; \epsilon) = -3.9009$ .

$i = 1$  to  $N$ . This eliminates radial fluctuations; the Monte-Carlo integral for  $\Phi_0$  is replaced with a panel integration uniformly spaced in  $M(r)$ , and the central potential is obtained with relatively high accuracy.

This trick does not suppress *non-radial* fluctuations, so the  $N$ -body potential evaluated at any point  $r > 0$  still differs from the true  $\Phi(r; \epsilon)$ . But a non-radial fluctuation which creates an overdensity at some position  $\mathbf{r}_{\text{over}}$  must borrow mass from elsewhere on the sphere  $r = |\mathbf{r}_{\text{over}}|$ ; over-dense and under-dense regions compensate each other when averaged over the entire surface of the sphere. The resulting potential fluctuations likewise average to zero over the sphere, as one can show by using Gauss's theorem to evaluate the average gradient of the potential and integrating inward from  $r = \infty$ .

Finally, a subtle bias arises if the particles used to generate the potential are also used to probe the potential, since local overdensities are sampled more heavily. To avoid this, the potential can be measured at a set of points  $\mathbf{r}_k$  which are *independent* of the particle positions  $\mathbf{r}_i$ . Then  $\delta\Phi_k \equiv \Phi_k - \Phi(r_k; \epsilon)$  should display some scatter, but average to zero when integrated over test points  $\mathbf{r}_k$  within a spherical shell.

Fig. 9 shows results from direct-sum potential calculations for tapered Hernquist and Jaffe models, using units with  $G = 1$ . In each case, the underlying density profile was represented with  $N = 2^{20} = 1048576$  equal-mass particles, and the potential was measured at 4096 points uniformly distributed in  $\log(r)$  between  $0.01\epsilon$  and  $100\epsilon$ . The points show results for uniform radial sampling. While non-radial fluctuations create scatter in  $\Phi_k$ , the distribution is fairly symmetric about the line  $\delta\Phi = 0$ . The jagged curves are obtained by averaging  $\delta\Phi_k$  over radial bins each containing 32 points. These averages fall near zero, demonstrating very good agreement between the  $N$ -body results and the potentials calculated from the smoothed density profiles.

For comparison, the grey-scale images in Fig. 9 display representative results for *random* realizations of each density profile. In these realizations, the radius of particle  $i$  is computed by solving  $M(r_i) = X_i M(\infty)$ , where  $X_i$  is a random number<sup>3</sup> uniformly distributed between 0 and 1. To examine the range of outcomes, 1000 random realizations of each model were generated and ranked by central potential  $\Phi_0$ ; since particle radii are chosen independently, the central limit theorem implies that  $\Phi_0$  has a normal distribution. Shown here are the 25<sup>th</sup> percentile and 75<sup>th</sup> percentile members of these ensembles; half of all random realizations lie between the two examples presented in each figure. Note that these examples deviate from the true potential by fractional amounts of  $\sim N^{-1/2}$ . Obviously, it's impossible to detect discrepancies between  $\Phi_k$  and  $\Phi(r_k; \epsilon)$  of less than one part in  $10^3$  using random realizations with  $N \sim 10^6$ .

It's instructive, not to mention disconcerting, to try reproducing Fig. 9 using a tree code (Barnes & Hut 1986) instead of direct summation. Tree codes employ approximations which become less accurate for  $\epsilon > 0$  (Hernquist 1987; Wachlin & Carpintero 2006); these systematically bias computed potentials and accelerations (see Appendix B). For example, the code

<sup>3</sup> A good random number generator is essential. The Unix generator, `random()`, appears to be slightly non-uniform; replacing  $X_i$  with  $1 - X_i$  yields systematically different  $\Phi_0$  values. The results shown here use the Tausworthe generator `taus2` (Galassi et al. 2009).



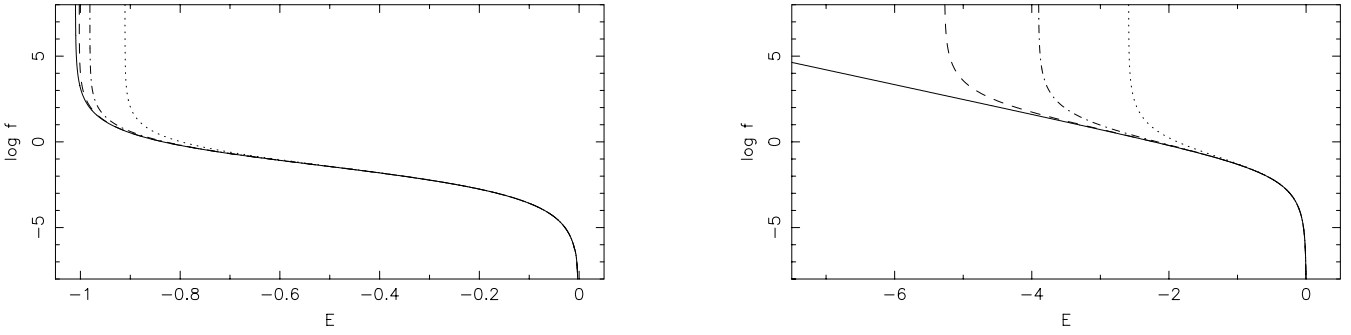


**Figure 10.** Distribution functions for tapered Hernquist (left) and Jaffe (right) models. Solid curve:  $f(E)$ ; dashed, dot-dashed, and dotted curves:  $f(E; \epsilon)$  for  $\epsilon = 1/256, 1/64$ , and  $1/16$ , respectively.

which will shortly be used for dynamical tests, run with an opening angle  $\theta = 0.8$ , yields central potentials which are too deep by a few parts in  $10^3$ , depending on the system being modeled. This systematic error cannot be ‘swept under the carpet’ when comparing computed and predicted potentials at the level of precision attempted here.

#### 4.2 Distribution functions

Constructing equilibrium configurations is an important element of many  $N$ -body experiments. Approximate equilibria may be generated by a variety of ad hoc methods, but the construction of a true equilibrium  $N$ -body model amounts to drawing particle positions and velocities from an equilibrium distribution function  $f = f(\mathbf{r}, \mathbf{v})$ . However, a configuration based on a distribution function (DF) derived without allowing for softening will *not* be in equilibrium if it is simulated with softening.

Assume the model to be constructed is spherical and isotropic. Broadly speaking, there are two options: (a) adopt a DF  $f = f(E)$  which depends on the energy  $E$ , and solve Poisson’s equation for the gravitational potential, or (b) adopt a mass model  $\rho = \rho(r)$ , and use Eddington’s (1916) formula to solve for the DF. If softening is taken into account, option (a) becomes somewhat awkward, since the source term for Poisson’s equation (7) is non-local<sup>4</sup>. On the other hand, option (b) is relatively straightforward (e.g., Kazantzidis, Magorrian, & Moore 2004).

Starting with a desired density profile  $\rho(r)$ , the first step is to compute the smoothed density and mass profiles  $\rho(r; \epsilon)$  and  $M(r; \epsilon)$ , respectively. Since  $M(r; \epsilon) \geq 0$  everywhere, equation (19) guarantees that the smoothed potential  $\Phi(r; \epsilon)$  is a monotonically increasing function of  $r$ . It is therefore possible to express the underlying density profile  $\rho(r)$  as a function of  $\Phi(r; \epsilon)$ , and compute the DF:

$$f(E; \epsilon) = \frac{1}{\sqrt{8\pi^2}} \frac{d}{dE} \int_E^0 d\Phi (\Phi - E)^{-1/2} \frac{d\rho}{d\Phi}. \quad (21)$$

Note that in  $d\rho/d\Phi$ , the quantity  $\rho = \rho(r)$  is the *underlying* density, while  $\Phi = \Phi(r; \epsilon)$  is the *smoothed* potential, related by Poisson’s equation to the smoothed density  $\rho(r; \epsilon)$ . In effect, the smoothed potential  $\Phi(r; \epsilon)$  is taken as a given, and (21) is used to find what will hereafter be called the *smoothed distribution function*  $f(E; \epsilon)$ ; with this DF, the underlying profile  $\rho(r)$  is in equilibrium in the adopted potential (e.g., McMillan & Dehnen 2007; Barnes & Hibbard 2009). Conversely, setting  $\epsilon = 0$  yields the *self-consistent distribution function*  $f(E)$  which describes a self-gravitating model with the underlying profile  $\rho(r)$ .

Fig. 10 presents DFs for tapered Hernquist and Jaffe models. In each case the solid line shows the self-consistent DF; these match the published DFs (Jaffe 1983; Hernquist 1990) over almost the entire energy range, deviating only for  $E \gtrsim -GM/b = -0.01$  where tapering sets in.

Smoothed DFs for Jaffe models appear very different from their self-consistent counterpart. The latter has a logarithmic, infinitely deep potential well, which effectively confines material with constant velocity dispersion in a  $\rho \propto r^{-2}$  cusp. The characteristic phase-space density  $f \sim \rho\sigma^{-3} \propto r^{-2}$  diverges as  $r \rightarrow 0$  (ie, as  $E \rightarrow -\infty$ ), but only because  $\rho$  does. With  $\epsilon > 0$  the potential well is harmonic at small  $r$ , and can’t confine a  $\rho \propto r^{-2}$  cusp unless the local velocity dispersion scales as  $\sigma \propto r$ ; thus the phase-space density now diverges as  $f \propto r^{-5}$ . Moreover, the domain of  $f(E; \epsilon)$  is limited to  $E_0 \leq E \leq 0$ , where  $E_0 \equiv \Phi(0; \epsilon)$ . Thus, instead of growing exponentially as a function of  $-E$ , the smoothed DF abruptly diverges at some finite energy.

By comparison, smoothed DFs for Hernquist models look similar to the self-consistent DF. The latter has a potential well of finite depth, and the smoothed profiles generate wells which are only slightly shallower. As the left panel of Fig. 10 shows, all the DFs asymptote to  $\infty$  as  $E \rightarrow E_0$ . However, the run of velocity dispersion with  $r$  is different; the self-consistent model has  $\sigma \propto r^{1/2}$ , implying  $f \propto \rho\sigma^{-3} \propto r^{-5/2}$ . In contrast, the smoothed models have  $\sigma \propto r$ , implying  $f \propto r^{-4}$ .

<sup>4</sup> Debattista & Sellwood (2000) describe an iterative scheme using softened  $N$ -body potentials which implements option (a).



One consequence is that the way in which  $f \rightarrow \infty$  as  $E \rightarrow E_0$  is different in the smoothed and self-consistent Hernquist models. The self-consistent model has a linear potential as small  $r$ , and thus  $f \propto r^{-5/2} \propto (E - E_0)^{-5/2}$ . By comparison, the models based on smoothed potentials have harmonic cores, and as a result,  $f \propto r^{-4} \propto (E - E_0)^{-2}$ . (This difference is not apparent in Fig. 10 but becomes obvious when  $\log(E - E_0)$  is plotted against  $\log f$ .) In this respect, the use of a smoothed potential effects a non-trivial change on Hernquist models:  $f$  is a different power-law of  $(E - E_0)$ . Coincidentally, the smoothed Jaffe models have  $f \propto r^{-5} \propto (E - E_0)^{-5/2}$ , just like the self-consistent Hernquist model.

### 4.3 Dynamical tests

$N$ -body simulations are useful to show that the distribution functions just constructed are actually in dynamical equilibrium with their smoothed potentials. For each model and  $\epsilon$  value, two ensembles of three random realizations were run. In one ensemble, the initial conditions were generated using the self-consistent DF  $f(E)$ . The other ensemble used initial conditions generated from the smoothed DF  $f(E; \epsilon)$ , which allows for the effects of softening.

Each realization contained  $N = 2^{18} = 262144$  equal-mass particles. Initial particle radii  $r_i$  were selected randomly by solving  $M(r_i) = X_i M(\infty)$  as described above. Initial particle speeds  $v_i$  were selected randomly by rejection sampling (von Neumann 1951) from the distributions  $g(v; r_i) = v^2 f(\frac{1}{2}v^2 + \Phi(r_i))$  or  $g(v; r_i) = v^2 f(\frac{1}{2}v^2 + \Phi(r_i; \epsilon); \epsilon)$ , where the former assumes the self-consistent DF, and the latter a smoothed DF. Position and velocity vectors for particle  $i$  are obtained by multiplying  $r_i$  and  $v_i$  by independent unit vectors drawn from an isotropic distribution. In effect, this procedure treats the 6-D distribution function  $f(\mathbf{r}, \mathbf{v})$  as a probability density, and selects each particle's coordinates independently.

Simulations were run using a hierarchical  $N$ -body code<sup>5</sup>. An opening angle of  $\theta = 0.8$ , together with quadrupole moments, provided forces with median errors  $\delta \mathbf{a}/|\mathbf{a}| \lesssim 0.0006$ . Particles within  $r \sim 10\epsilon$  have much larger force errors, although these seem to have limited effect in practice (Appendix B). Trajectories were integrated using a time-centered leap-frog, with the same time-step  $\Delta t = 1/1024$  for all particles (see § 4.3.1). All simulations were run to  $t = 16$ , which is more than sufficient to test initial equilibrium.

Fig. 11 shows how the potential well depth  $\Phi_{\min}$  of each simulation evolves as a function of time. Here, well depth is estimated by computing the softened gravitational potential  $\Phi_i$  of each particle  $i$  and taking the minimum (most negative) value. (This is more accurate than evaluating the potential at the origin since the center of the system may wander slightly during a dynamical simulation.) To better display the observed changes in  $\Phi_{\min}$ , the horizontal axis is logarithmic in time.

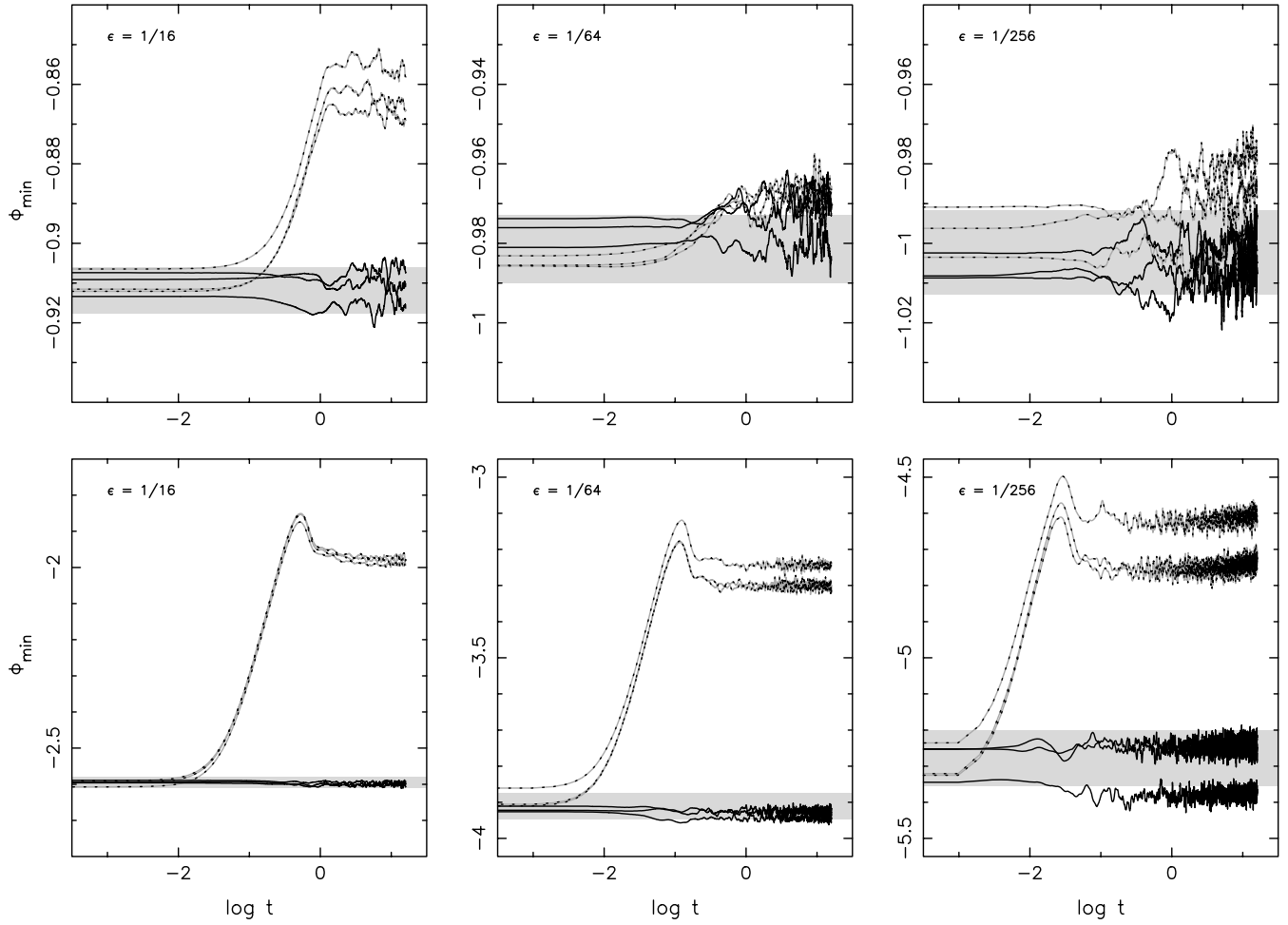
Most of the ensembles set up without allowing for softening (dotted curves in Fig. 11) are clearly not in equilibrium. In all three of the Jaffe models (bottom row), the potential wells become dramatically shallower on a time-scale comparable to the dynamical time at  $r = \epsilon$ . The reason for this is evident. The self-consistent Jaffe model has a central potential diverging like  $\log r$  as  $r \rightarrow 0$ ; this potential can confine particles with finite velocity dispersion at arbitrarily small radii. However, the relatively shallow potential well of a smoothed Jaffe model cannot confine these particles; they travel outward in a coherent surge and phase-mix at radii of a few  $\epsilon$ . Their outward surge and subsequent fallback accounts for the rapid rise and partial rebound of the central potential. Similar although less pronounced evolution occurs in the Hernquist models (top row) with  $\epsilon = 1/16$  and possibly with  $\epsilon = 1/64$  as well. Only the self-consistent Hernquist models run with  $\epsilon = 1/256$  appear truly close to equilibrium.

In contrast, all of the ensembles set up with smoothed DFs (solid curves in Fig. 11) are close to dynamical equilibrium. In equilibrium, gravitational potentials fluctuate as individual particles move along their orbits. If particles are uncorrelated, the amplitude of these fluctuations should be comparable to the amplitude seen in an ensemble of independent realizations. To check this, 1000 realizations of each model were generated; central gravitational potentials  $\Phi_{\min}$  were evaluated using the same tree algorithm and parameters used for the self-consistent simulations. The grey horizontal bands show a range of  $\pm 2\sigma$  around the average central potential for each model and choice of  $\epsilon$ . Some of the simulations set up using smoothed DFs wander slightly beyond the  $2\sigma$  range. However, none of them exhibit the dramatic evolution seen in the cases set up using self-consistent DFs.

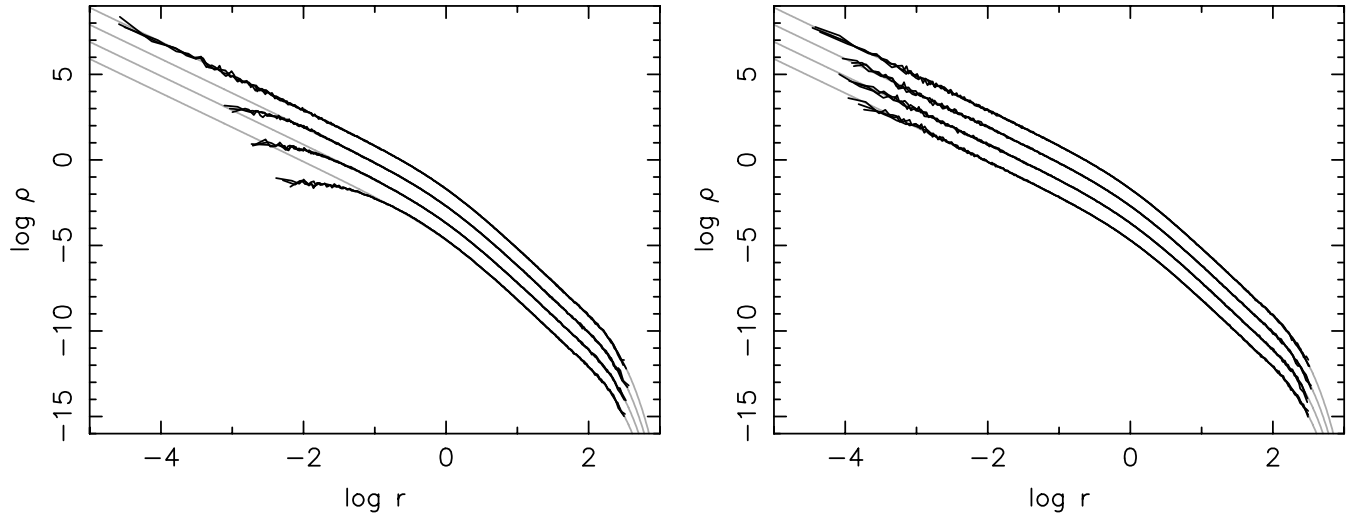
The central potential is relatively insensitive to changes in the mass distribution on scales  $r \ll \epsilon$ . To examine small-scale changes directly, density profiles measured from the initial conditions were compared to profiles measured at  $t = 16$  time units. These profiles were derived as follows. First, SPH-style interpolation with an adaptive kernel containing 32 particles was used to estimate the density around each particle. Next, the centroid position  $\mathbf{r}_{\text{cent}}$  of the 32 highest-density particles was determined. Finally, a set of nested spherical shells, centered on  $\mathbf{r}_{\text{cent}}$ , were constructed; each shell was required to contain at least 16 particles and have an outer radius at least 1.05 times its inner radius.

Fig. 12 summarizes results for Jaffe models, which display the most obvious changes. The density of each shell is plotted against the average distance from  $\mathbf{r}_{\text{cent}}$  of the particles it contains. In each panel, the top set of curves compare initial ( $t = 0$ ) numerical results with the underlying tapered Jaffe model, always represented by a light grey line. Profiles from three

<sup>5</sup> See <http://www.ifa.hawaii.edu/faculty/barnes/treecode/treeguide.html> for a description.



**Figure 11.** Evolution of potential well depth for  $N$ -body simulations of Hernquist (top row) and Jaffe (bottom row) models, each run with the  $\epsilon$  value labeled. Solid (dotted) curves show results for initial conditions generated from smoothed (self-consistent) DFs. Light grey bands show expected  $\pm 2\sigma$  variation in central potential for  $N = 262144$  independent particles.



**Figure 12.** Density profiles of Jaffe models before and after dynamical evolution. Initial conditions were constructed using self-consistent DFs (left) and smoothed DFs (right). In each panel, the top profile shows the initial conditions; the smooth curve is the underlying tapered model, overplotted by three slightly bumpy curves showing numerical results from three independent realizations. The three profiles below show numerical results at  $t = 16$  for simulations run with  $\epsilon = 1/256$ ,  $1/64$ , and  $1/16$ , respectively; each is displaced downward by one additional unit in  $\log \rho$  for clarity.

independent  $N$ -body realizations of each model are overplotted. While some scatter from realization to realization is seen, the measured densities track the underlying profile throughout the entire range plotted. The outermost point is at  $\sim 10^7$  times the radius of the innermost one; there are not enough particles to obtain measurements at smaller or larger radii.

Ranged below the top curves in Fig. 12 are numerical results at  $t = 16$  for softening lengths  $\epsilon = 1/256$ ,  $1/64$ , and  $1/16$ , each shifted downward by one more unit in  $\log \rho$ . Again, profiles from three independent simulations are overplotted to illustrate run-to-run variations. Simulations set up using the self-consistent DF (left panel) show significant density evolution; their initial power-law profiles are rapidly replaced by cores of roughly constant density inside  $r \lesssim \epsilon$ . In contrast, simulations set up using smoothed DFs (right panel) follow the initial profile down to  $r \sim 10^{-4}$  (although density evolution occurs on smaller scales). This shows that a careful set-up procedure can maintain the initial density profile even on scales much smaller than the softening length.

A similar plot for the Hernquist models confirms that most of these simulations start close to equilibrium. Hernquist models set up using smoothed DFs don't appear to evolve at all, although this statement should be qualified since the profiles of these models can't be measured reliably on scales much smaller than  $r \sim 10^{-2}$ . Models set up using the self-consistent DF and run with  $\epsilon = 1/16$  undergo some density evolution; their profiles fall below the underlying Hernquist model at  $r \sim \epsilon$ , although they continue rising to the innermost point measured. Simulations run with  $\epsilon = 1/64$  or less display no obvious changes down to scales of  $r \sim 10^{-2}$ .

It appears that the Jaffe models set up using smoothed DFs are not *completely* free of long-term evolution. The right-hand panel of Fig. 12 shows that the peak density as measured using a fixed number of particles falls by roughly an order of magnitude by  $t = 16$ . Moreover, a close examination of Fig. 11 turns some cases with a gradual decrease in potential well depth; in the smoothed Jaffe models with  $\epsilon = 1/256$ , for example,  $\Phi_{\min}$  exhibits an upward trend of  $\sim 0.011$  percent per unit time. This evolution may not be due to any flaw in the initial conditions; the central cusps of such models, which are confined by *very* shallow harmonic potentials, are fragile and easily disrupted. There may be more than one mechanism at work here; the rate of potential evolution appears to be inversely proportional to particle number  $N$ , while the rate of density evolution is independent of  $N$ . A full examination of this matter is beyond the scope of this paper.

#### 4.3.1 Choice of time-step

Selecting the time-step  $\Delta t$  for an  $N$ -body simulation is a non-trivial problem. While the choice can usually be justified post-hoc by testing for convergence in a series of experiments with different time-steps, it's clearly convenient to be able to estimate an appropriate  $\Delta t$  a priori. A general rule governing such estimates is that the time-step should be smaller than the shortest dynamical time-scale present in the simulation.

The central density  $\rho_c = \rho(0; \epsilon)$  of a smoothed density profile defines one such time-scale. Within the nearly constant-density core of a smoothed profile, the local orbital period is  $t_c = \sqrt{3\pi/G\rho_c}$ ; this is the shortest orbital period anywhere in the system. Numerical tests show the leap-frog integrator is well-behaved if  $\Delta t \lesssim 0.05t_c$  (conversely, it becomes unstable if  $\Delta t \gtrsim 0.15t_c$ ). Among the models simulated here, the Jaffe model with  $\epsilon = 1/256$  has the highest smoothed central density; for this model,  $\rho_c = \rho_J(0; \epsilon) \simeq D_0(2)\rho_J(\epsilon) = 10440$ . Given this density,  $t_c \simeq 0.0300$  and  $\Delta t \lesssim 0.0015$ .

The time required for a fast-moving particle to cross the core region defines another time-scale. If  $\Phi_c = \Phi(0; \epsilon)$  is depth of the central potential well, the maximum speed of a bound particle is  $\sqrt{-2\Phi_c}$ , and the core crossing time is  $t_x = \epsilon/\sqrt{-2\Phi_c}$ . The smoothed Jaffe model with  $\epsilon = 1/256$  has the deepest potential well. For this model, tests of the leap-frog with fast-moving particles on radial orbits show that  $\Delta t \leq t_x \simeq 0.0012$  yields good results, but time-steps a few times longer result in poor energy conservation as particles traverse the core region. (The relationship between  $t_x$  and the maximum acceptable time-step  $\Delta t$  may be somewhat model-dependent.)

Thus, for the Jaffe model with  $\epsilon = 1/256$ , both the local criterion based on  $t_c$  and the global criterion based on  $t_x$  yield similar constraints<sup>6</sup> on  $\Delta t$ . It's convenient to round  $\Delta t$  down to the next power of two, implying  $\Delta t = 1/1024$ . This corresponds to  $\Delta t \simeq 0.03t_c \simeq 0.81t_x$ , which is somewhat conservative but helps insure that non-equilibrium changes will be accurately followed.

To see if this time-step is reasonable, realizations of this model were simulated with various values of  $\Delta t$  between  $1/128$  to  $1/2048$ . At the lower end of this range, the effects of an over-large time-step manifest quickly; global energy conservation is violated, and the measured central potential  $\Phi_{\min}$  drifts upward over time (even though the initial conditions, generated from  $f(E; \epsilon)$ , are near equilibrium). With a time-step  $\Delta t = 1/128$ , for example; the potential well becomes  $\sim 3$  percent shallower during the first two time-steps, and by  $t = 4$  its depth has decreased by 18 percent. These simulations also violate global energy conservation, becoming  $\sim 4.5$  percent less bound by  $t = 4$ . Integration errors are reduced – but not entirely eliminated – with a time-step  $\Delta t = 1/256$ ; by  $t = 4$ , the potential well becomes  $\sim 1.3$  percent shallower, while total energy changes by

<sup>6</sup> Assuming  $\epsilon \ll a$ , one can show that  $t_c/t_x \simeq 11\sqrt{\ln(a/\epsilon)}$  for any smoothed Jaffe model; both criteria yield similar constraints almost independent of  $\epsilon$ . For smoothed Hernquist models, on the other hand,  $t_c/t_x \simeq 11\sqrt{a/\epsilon}$ ; the constraint based on  $t_x$  is generally stricter.

$\sim 0.4$  percent. With a time-step of  $\Delta t = 1/512$  or less, global energy conservation is essentially perfect, and variations in  $\Phi_{\min}$  appear to be driven largely by particle discreteness as opposed to time-step effects.

Plots analogous to Fig. 12 show that the simulations with time-steps as large as  $\Delta t = 1/256 \simeq 0.12t_c$  reproduce the inner cusps of Jaffe models just as well as those with  $\Delta t = 1/1024$ . With this time-step, individual particles may not be followed accurately, but their aggregate distribution is not obviously incorrect. On the other hand, a time-step  $\Delta t = 1/128$  yields density profiles which fall below the initial curves for  $r \lesssim 0.01$ .

## 5 DISCUSSION

Softening and smoothing are mathematically equivalent. While the particular form of softening adopted in (4) corresponds to smoothing with a Plummer kernel (5), other softening prescriptions can also be described in terms of smoothing operations (e.g. Dehnen 2001). There are two conceptual advantages to thinking about softening as a smoothing process transforming the underlying density field  $\rho(\mathbf{r})$  to the smoothed density field  $\rho(\mathbf{r}; \epsilon)$ . First, since the gravitational potential  $\Phi(\mathbf{r}; \epsilon)$  is related to  $\rho(\mathbf{r}; \epsilon)$  by Poisson's equation, the powerful mathematical machinery of classical potential theory becomes available to analyze potentials in  $N$ -body simulations. Second, focusing attention on smoothing makes the source term for the gravitational field explicit. From this perspective, smoothing is not a property of the particles, but a separate step introduced to ameliorate  $1/r$  singularities in the potential. Particle themselves are points rather than extended objects; this insures that their trajectories are characteristics of (1).

Plummer smoothing converts  $\rho_n(r) \propto r^{-n}$  power-laws to cores. At radii  $r \gg \epsilon$  the density profile is essentially unchanged, while at  $r \ll \epsilon$  the density approaches a constant value equal to the density of the underlying model at  $r = \epsilon$  times a factor which depends only on  $n$ . For the case  $n = 1$ , this factor is unity and  $\rho_1(r; \epsilon) = \rho_1(\sqrt{r^2 + \epsilon^2})$  everywhere.

The effects of Plummer smoothing on astrophysically-motivated models with power-law cusps, such as the Jaffe, Hernquist, and NFW profiles, follow for the most part from the results for pure power-laws. In particular, for  $\epsilon \lesssim a/64$ , where  $a$  is the profile's scale radius, the power-law results are essentially 'grafted' onto the underlying profile. On the other hand, for  $\epsilon \gtrsim a/16$ , the inner power-law is erased by smoothing.

Smoothing provides a way to predict the potentials obtained in  $N$ -body calculations to an accuracy limited only by  $\sqrt{N}$  fluctuations. These predictions offer new and powerful tests of  $N$ -body methodology, exposing subtle systematic effects which may be difficult to diagnose by other means.

Given an underlying density profile  $\rho(r)$ , it's straightforward to construct an isotropic distribution function  $f(E; \epsilon)$  such that  $\rho(r)$  is in equilibrium with the potential generated by its smoothed counterpart  $\rho(r; \epsilon)$ . Such distribution functions can be used to generate high-quality equilibrium initial conditions for  $N$ -body simulations; they should be particularly effective when realized with 'quiet start' procedures (Debattista & Sellwood 2000). Systems with shallow central cusps, such as Hernquist and NFW models, may be set up fairly close to equilibrium without taking softening into account as long as  $\epsilon$  is not too large. However, it appears impossible to set up a good  $N$ -body realization of a Jaffe model without allowing for softening.

It's true that realizations so constructed don't reproduce the actual dynamics of the underlying models at small radii (Dehnen 2001, footnote 8); to obtain an equilibrium, the velocity dispersion is reduced on scales  $r \lesssim \epsilon$ . But realizations set up *without* softening preserve neither the dispersion nor the density at small radii, and the initial relaxation of such a system can't be calculated a priori but must be simulated numerically. On the whole, it seems better to get the central density profile right on scales  $r < \epsilon$ , and know how the central velocity dispersion profile has been modified. Even if the dynamics are not believable within  $r \lesssim \epsilon$ , the ability to localize mass on such scales may be advantageous in modeling dynamics on larger scales.

Mathematica code to tabulate smoothed models is available at

<http://www.ifa.hawaii.edu/faculty/barnes/research/smoothing/>.

## ACKNOWLEDGMENTS

I thank Jun Makino and Lars Hernquist for useful and encouraging comments, and an anonymous referee for a positive and constructive report. Mathematica rocks.

## REFERENCES

- Athanassoula, E., Bosma, A., Lambert, J.-C., Makino, J. 1998, 'Performance and accuracy of a GRAPE-3 system for collisionless N-body simulations', *MNRAS*, **293**, 369–380
- Athanassoula, E., Fady, E., Lambert, J.-C., Bosma, A. 2000, 'Optimal softening for force calculations in collisionless N-body simulations', *MNRAS*, **314**, 475–488

- Barnes, J.E. 1998, ‘Dynamics of Galaxy interactions’, in *Galaxies: Interactions and Induced Star Formation*, eds. D. Friedli, L. Martinet, & D. Pfenniger. Berlin, Springer, p. 275–394
- Barnes, J. & Hut, P. 1986, ‘A hierarchical  $O(N \log N)$  force-calculation algorithm’, *Nature*, **324**, 446–449
- Barnes, J. & Hut, P. 1989, ‘Error analysis of a tree code’, *ApJS*, **70**, 389–417
- Barnes, J.E. & Hibbard, J.E. 2009, ‘IDENTIKIT 1: A modeling tool for interacting disc galaxies’, *AJ*, **137**, 3071–3090
- Debattista, V.P. & Sellwood, J.A. 2000, ‘Constraints from Dynamical Friction on the Dark Matter Content of Barred Galaxies’, *ApJ*, **543**, 704–721
- Dehnen, W. 2001, ‘Towards optimal softening in three-dimensional  $N$ -body codes – I. Minimizing the force error’, *MNRAS*, **324**, 273–291
- Dyer, C.C. & Ip, P.S.S. 1993, ‘Softening in  $N$ -body simulations of collisionless systems’, *ApJ*, **409**, 60–67
- Eddington, A.S. 1916, ‘The distribution of stars in globular clusters’, *MNRAS*, **76**, 572–585
- Hernquist, L. & Barnes, J.E. 1990, ‘Are some  $N$ -body algorithms intrinsically less collisional than others?’, *ApJ*, **349**, 562–569
- Galassi, M., Davies, J., Theiler, J., Gough, B., Jungman, G., Alken, P., Booth, M., Rossi, F. 2009, ‘GNU Scientific Library Reference Manual’, Network Theory Ltd, UK
- Hernquist, L.E. 1987, ‘Performance Characteristics of Tree Codes’, *ApJS*, **64**, 715–734
- Hernquist, L.E. 1990, ‘An analytical model for spherical galaxies and bulges’, *ApJ*, **356**, 359–364
- Jaffe, W. 1983, ‘A simple model for the distribution of light in spherical galaxies’, *MNRAS*, **202**, 995–999
- Kazantzidis, S., Magorrian, J., & Moore, B. 2004, ‘Generating Equilibrium Dark Matter Halos: Inadequacies of the Local Maxwellian Approximation’, *ApJ*, **601**, 37–46
- Klimontovich, Yu. L. 1967, ‘The statistical theory of non-equilibrium processes in a plasma’, M.I.T. Press, Cambridge, MA.
- McMillan, P.J. & Dehnen, W. 2007, ‘Initial conditions for disc galaxies’, *MNRAS*, **378**, 541–550
- Merritt, D. 1996, ‘Optimal Smoothing for N-Body Codes’, *AJ*, **111**, 2462–2464
- Navarro, J.F., Frenk, C.S., & White, S.D.M. 1996, ‘The Structure of Cold Dark Matter Halos’, *ApJ*, **462**, 563–575
- Plummer, H.C. 1911, ‘On the problem of distribution in globular star clusters’, *MNRAS*, **71**, 460–470
- von Neumann, J. 1951, ‘Various techniques used in connection with random digits’, in *Monte Carlo Method*, eds. A.S. Householder, G.E. Forsythe, & H.H. Germond. National Bureau of Standards Applied Mathematics Series **12**, U.S. Government Printing Office, Washington, D.C., p. 36–38
- Wachlin, F.C. & Carpintero, D.D. 2006, ‘Softened potentials and the multipolar expansion’, *Rev. Mex. Astr. Ap.*, **42**, 251–259

## APPENDIX A: APPROXIMATIONS

### A.1 Power-law profiles

The power-law density and cumulative mass profiles are

$$\rho_n(r) = \rho_a \left(\frac{a}{r}\right)^n, \quad M_n(r) = \frac{4\pi}{3-n} \rho_a a^n r^{(3-n)}. \quad (22)$$

Plummer smoothing converts power laws with  $n < 3$  to finite-density cores. At  $r \ll \epsilon$  the smoothed density is nearly constant and close to the smoothed central density  $\rho_n(0; \epsilon) = D_0(n) \rho_n(\epsilon)$ . Within this constant-density region, the smoothed mass profile is approximately

$$\overline{M}_n(r; \epsilon) = \frac{4\pi}{3} r^3 \rho_n(0; \epsilon) = \frac{4\pi}{3} r^3 D_0(n) \rho_a \left(\frac{a}{\epsilon}\right)^n. \quad (23)$$

At  $r \gg \epsilon$ , on the other hand, smoothing has little effect on the mass profile, so  $M_n(r; \epsilon) \simeq M_n(r)$ . Interpolating between these functions yields an approximate expression for the smoothed mass profile:

$$\tilde{M}_n(r; \epsilon) = \left( \overline{M}_n(r; \epsilon)^{-\kappa/n} + M_n(r)^{-\kappa/n} \right)^{-n/\kappa}, \quad (24)$$

where the shape parameter  $\kappa$  determines how abruptly the transition from one function to the other takes place. This expression can be rearranged to give

$$\tilde{M}_n(r; \epsilon) = \left( \left( \frac{3}{(3-n)D_0(n)} \right)^{\kappa/n} \left( \frac{\epsilon}{r} \right)^\kappa + 1 \right)^{-n/\kappa} M_n(r). \quad (25)$$

The smoothed density profile is obtained by differentiating the mass profile:

$$\tilde{\rho}_n(r; \epsilon) = \frac{1}{4\pi r^2} \frac{d}{dr} \tilde{M}_n(r; \epsilon). \quad (26)$$

Figs. 13 and 14 present tests of these approximations for  $\rho \propto r^{-1}$  and  $r^{-2}$  power-laws, respectively. As in Figs. 1 and 2, the smoothed density profile was computed with  $\epsilon = 1$ ; for other values of  $\epsilon$ , the entire pattern simply shifts left or right

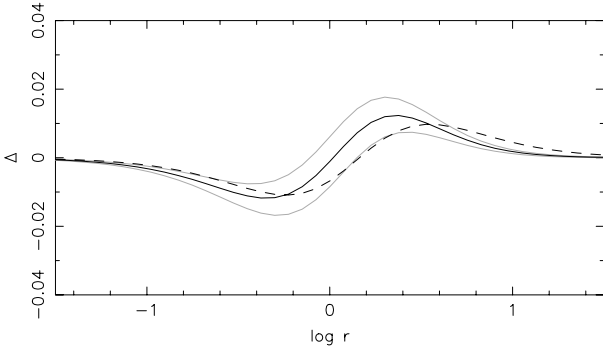


**Figure 13.** Relative error in smoothed density (solid) and mass (dashed) for a  $\rho \propto r^{-1}$  profile, computed for  $\epsilon = 1$  using (25) and (26). Dark curves show results for  $\kappa = 1.739$ ; light grey solid curves show errors in density only for  $\kappa = 1.769$  (above) and  $\kappa = 1.709$  (below).

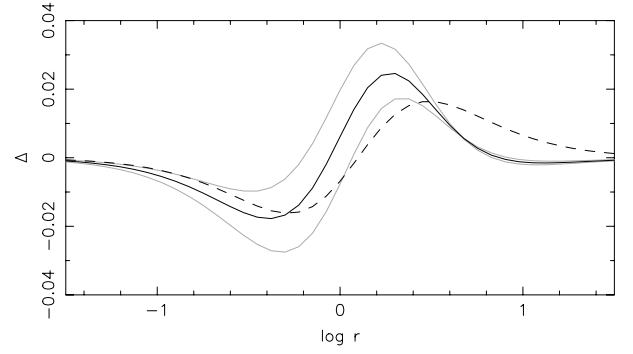


**Figure 14.** Relative error in smoothed density (solid) and mass (dashed) for a  $\rho \propto r^{-2}$  profile, computed for  $\epsilon = 1$  using (25) and (26). Dark curves show results for  $\kappa = 1.820$ ; light grey solid curves show errors in density only for  $\kappa = 1.850$  (above) and  $\kappa = 1.790$  (below).

without changing shape or amplitude. Dashed curves show relative errors in smoothed mass,  $\Delta_M = \tilde{M}(r; \epsilon)/M(r; \epsilon) - 1$ , while solid curves are relative errors in smoothed density  $\Delta_\rho = \tilde{\rho}(r; \epsilon)/\rho(r; \epsilon) - 1$ . The  $\kappa$  value used for each dark curve is the value which minimizes  $\sum_i \Delta_\rho(r_i)^2$  evaluated at points  $r_i$  distributed uniformly in  $\log r$  between  $\log r = -1.5$  and  $1.5$ . In light grey, plots of  $\Delta_\rho(r)$  for two other  $\kappa$  illustrate the sensitivity to this parameter. Comparing these plots, it appears that the approximation works better for the  $\rho \propto r^{-1}$  power-law than it does for  $r^{-2}$ , but even in the latter case the maximum error is only  $\sim 2\%$ .

Because (25) modifies the underlying mass profile with a multiplicative factor, it can also be used to approximate effects of softening on non-power-law profiles (e.g. Barnes & Hibbard 2009); for this purpose, both  $\epsilon$  and  $\kappa$  can be treated as free parameters and adjusted to provide a good fit. The resulting errors in density, which amount to a few percent near the softening scale, are undesirable but don't appear to seriously compromise  $N$ -body simulations with  $N \sim 10^5$ .

## A.2 Hernquist and NFW profiles

For  $\epsilon \ll a$ , smoothing primarily modifies the  $r^{-1}$  part of these density profiles. This, together with the exact solution for the case  $\rho \propto r^{-1}$  given in § 2.1, suggests simple approximations for smoothed Hernquist and NFW models:

$$\tilde{\rho}_H(r; \epsilon) = \rho_H(\sqrt{r^2 + \epsilon^2}) = \rho_H(r_\epsilon), \quad \tilde{\rho}_{\text{NFW}}(r; \epsilon) = \rho_{\text{NFW}}(\sqrt{r^2 + \epsilon^2}) = \rho_{\text{NFW}}(r_\epsilon). \quad (27)$$

Fig. 15 plots the relative error in density,  $\Delta_\rho = \tilde{\rho}(r; \epsilon)/\rho(r; \epsilon) - 1$  for both models, adopting  $\epsilon = a/16$ . For other values of  $\epsilon$ , these errors scale roughly as  $\epsilon^{1.6}$ .

The general behavior of these approximations is readily understood. Overall,  $\tilde{\rho}_{\text{NFW}}(r; \epsilon)$  is more accurate than  $\tilde{\rho}_H(r; \epsilon)$  since the NFW profile is closer to  $\rho \propto r^{-1}$  at all radii. Both curves are approximately flat for  $r \ll \epsilon$ , then reach minima for  $r$  between  $\epsilon$  and the profile scale radius  $a$ . These minima arise because the smoothed density approaches or even slightly exceeds the underlying density (see Figs. 4 and 5), while (27) always yields values below the underlying density.

It's sometimes useful to have the cumulative mass for a smoothed profile. The approximate profiles in (27) can be integrated analytically, although the resulting expressions are a bit awkward:

$$\begin{aligned} \tilde{M}_H(r; \epsilon) &= \int_0^r dx 4\pi x^2 \tilde{\rho}_H(x; \epsilon) \\ &= \frac{\epsilon^2 a M}{(\epsilon^2 - a^2)^{3/2}} \left( \arctan\left(\frac{r}{\sqrt{\epsilon^2 - a^2}}\right) - \arctan\left(\frac{ar}{r_\epsilon \sqrt{\epsilon^2 - a^2}}\right) - \frac{r\sqrt{\epsilon^2 - a^2}(a^3 r_\epsilon - a^2(\epsilon^2 + 2r^2) + ar_\epsilon(r^2 - \epsilon^2) + \epsilon^2 r_\epsilon^2)}{\epsilon^2(r_\epsilon^2 - a^2)^2} \right) \end{aligned} \quad (28)$$

and

$$\begin{aligned} \tilde{M}_{\text{NFW}}(r; \epsilon) &= \int_0^r dx 4\pi x^2 \tilde{\rho}_{\text{NFW}}(x; \epsilon) \\ &= 4\pi a^3 \rho_a \left( \frac{r(a - r_\epsilon)}{r_\epsilon^2 - a^2} + \frac{a}{\sqrt{\epsilon^2 - a^2}} \left( \arctan\left(\frac{ar}{r_\epsilon \sqrt{\epsilon^2 - a^2}}\right) - \arctan\left(\frac{r}{\sqrt{\epsilon^2 - a^2}}\right) \right) + \log\left(\frac{r + r_\epsilon}{\epsilon}\right) \right) \end{aligned} \quad (29)$$

Note that because the approximate profiles (27) systematically underestimate the true smoothed densities, these expressions will likewise systematically underestimate the total smoothed mass.



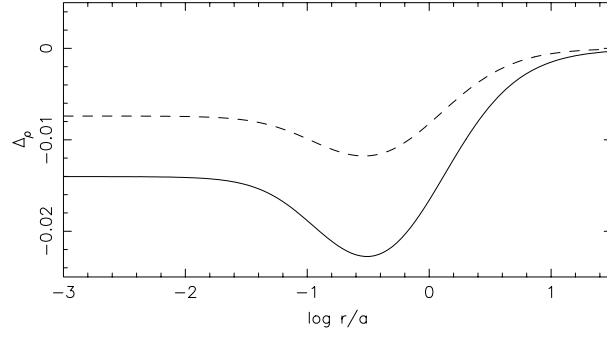


**Figure 15.** Relative error in density,  $\Delta\rho = \tilde{\rho}/\rho - 1$ , plotted vs. radius  $r$ , for the approximations given in (27). Solid and dashed curves show results for Hernquist and NFW profiles, respectively, computed for  $\epsilon = a/16$ .

## APPENDIX B: FORCE CALCULATION ERRORS

Tree codes reduce the computational cost of gravitational force calculation by making explicit approximations (Barnes & Hut 1986). The long-range potential due to a localized mass distribution  $\mathcal{M}$  with total mass  $M$  and center of mass position  $\mathbf{r}_0$  is approximated as

$$\Phi(\mathbf{r}) = -\frac{GM}{|\mathbf{r} - \mathbf{r}_0|} + \text{higher order terms}, \quad (30)$$

where the higher order terms include quadrupole and possibly higher-order moments (dipole terms vanish because  $\mathbf{r}_0$  coincides with the center of mass). To implement softening, this approximation is typically replaced with

$$\Phi(\mathbf{r}) = -\frac{GM}{\sqrt{|\mathbf{r} - \mathbf{r}_0|^2 + \epsilon^2}} + \text{higher order terms}. \quad (31)$$

This works at large distances, but becomes inaccurate if  $|\mathbf{r} - \mathbf{r}_0| \sim \epsilon$  (Hernquist 1987). Moreover, because the error is introduced at the *monopole* level (Wachlin & Carpintero 2006), higher-order corrections don't repair the damage.

To appreciate the problem, consider a sphere  $\mathcal{S}$  centered on  $\mathbf{r}_0$  with radius  $R$  large enough to enclose  $\mathcal{M}$ . For  $\epsilon = 0$ , the inward acceleration averaged over the surface of  $\mathcal{S}$  is easily computed using Gauss's theorem:

$$\bar{a}_r \equiv \frac{1}{4\pi R^2} \int_{\partial\mathcal{S}} d\mathbf{A} \cdot \mathbf{a} = -\frac{GM}{R^2}. \quad (32)$$

In other words, the monopole term is sufficient to calculate the inward acceleration averaged over the surface of  $\mathcal{S}$  *exactly*.

Suppose we want to compute  $\bar{a}_r$  for  $\epsilon > 0$ . Again using Gauss's theorem, we have

$$\bar{a}_r = -\frac{GM_S(\epsilon)}{R^2}, \quad \text{where} \quad M_S(\epsilon) = \int_{\mathcal{S}} d\mathbf{r} \rho(\mathbf{r}; \epsilon) \quad (33)$$

is the smoothed mass within the sphere. As before, this is an exact equality. The tree code approximation (31) implies that the enclosed mass is

$$M_S^0(\epsilon) = \frac{M}{(1 + \epsilon^2/R^2)^{3/2}}. \quad (34)$$

This is correct if  $\mathcal{M}$  is simply a point mass located at  $\mathbf{r}_0$ . But if  $\mathcal{M}$  has finite extent, then the enclosed mass  $M_S(\epsilon)$  is *always* less than  $M_S^0(\epsilon)$ . As a result, (31) will systematically *overestimate* the inward acceleration and depth of the potential well due to  $\mathcal{M}$ . Wachlin & Carpintero (2006) demonstrate a similar result by computing the softened potential of a homogeneous sphere; they find  $-GM/\sqrt{|\mathbf{r} - \mathbf{r}_0|^2 + \epsilon^2}$  is only the first term in a series.

The inequality  $M_S(\epsilon) < M_S^0(\epsilon)$  is easily verified for Plummer softening. An analogous inequality is likely to hold for other smoothing kernels  $S(r; \epsilon)$  which monotonically decrease with  $r$ . Smoothing kernels with compact support (Dehnen 2001) may be better behaved in this regard.

Under what conditions are these errors significant? For 'reasonable' values of  $\epsilon$ , most dynamically relevant interactions are on ranges  $\Delta r \gg \epsilon$  where softening has little effect; these interactions are not compromised since (31) is nearly correct at long range. Only if a significant fraction of a system's mass lies within a region of size  $\epsilon$  can these errors become important. This situation was not investigated in early tree code tests (e.g., Hernquist 1987; Barnes & Hut 1989), which generally used mass models with cores instead of central cusps, and even heavily softened Hernquist models don't have much mass within one softening radius. On the other hand, Jaffe models pack more mass into small radii; a Jaffe model with  $\epsilon = a/16$  has almost 6 percent of its mass within  $r = \epsilon$ . Jaffe models should be good test configurations for examining treecode softening errors.

Tests were run using tapered Jaffe and Hernquist models, realized using the same parameters ( $a = 1$ ,  $b = 100$ ,  $M = 1$ , and  $N = 262144$ ) used in the dynamical experiments (§ 4.3). In each model, the gravitational field was sampled at 4096 points



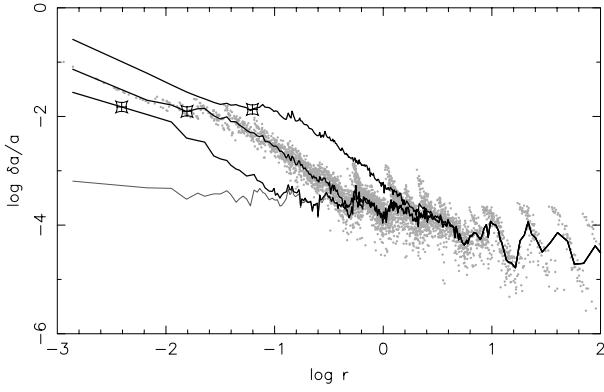


**Figure 16.** Tree code acceleration error  $\delta a/a$  plotted against radius. These results were obtained for a Jaffe model with  $\theta = 0.8$ . Grey dots show errors for individual test points with  $\epsilon = 1/64$ ; the jagged curve threading the dots is constructed by averaging points in groups of 16. Similar curves above and below show results for  $\epsilon = 1/16$  and  $\epsilon = 1/256$ , respectively. The large marker on each curve shows the average value of  $\delta a/a$  at radius  $r = \epsilon$ . The light grey curve shows results for  $\epsilon = 0$ .

drawn from the same distribution as the mass. At each test point, results from the tree code with opening angle  $\theta = 0.8$ , including quadrupole terms, were compared with the results of a direct-sum code. As expected, the tests with Hernquist models showed relatively little trend of force calculation error with  $\epsilon$ , although the errors are somewhat larger for  $\epsilon = 1/16$  than for smaller values. In contrast, the tests with Jaffe models reveal a clear relationship between softening length and force calculation accuracy.

Fig. 16 shows the relative acceleration error  $\delta a/a = |\mathbf{a}_t - \mathbf{a}_d|/|\mathbf{a}_d|$  for Jaffe models with various values of  $\epsilon$ . Here  $\mathbf{a}_t$  and  $\mathbf{a}_d$  are accelerations computed using a tree code and direct summation, respectively. The grey dots represent measurements of  $\delta a/a$  for individual test points, computed using  $\epsilon = 1/64$ . The pattern of errors suggests two regimes. At radii  $r \gtrsim 0.25$  ( $\log r \gtrsim -0.4$ ), the points fall in a ‘sawtooth’ pattern which reflects the hierarchical cell structure used in the force calculation. At smaller radii, on the other hand, the relative error grows more or less monotonically as  $r \rightarrow 0$ . It appears that errors in the large- $r$  regime are due to neglect of moments beyond quadrupole order in computing the potentials of individual cells; conversely, the errors in the small- $r$  regime are due to the tree code’s inaccurate treatment of softening. The direction of the error vectors  $\mathbf{a}_t - \mathbf{a}_d$  supports this interpretation; in the large- $r$  regime they are isotropically distributed, while in the small- $r$  regime they point toward the center of the system.

The jagged line threading through the dots in Fig. 16, constructed by averaging test points in groups of 16, shows the overall relationship between acceleration error and radius for  $\epsilon = 1/64$ . Similar curves are also plotted for  $\epsilon = 1/16$  (above) and  $\epsilon = 1/256$  (below). At large radii, all three curves coincide precisely, implying that force errors are independent of  $\epsilon$ . Going to smaller  $r$ , the curve for  $\epsilon = 1/16$  is the first to diverge, rising above the other two, next the curve for  $\epsilon = 1/64$  begins to rise, tracking the mean distribution of the plotted dots, and finally the curve for  $\epsilon = 1/256$  parallels the other two. Each curve begins rising monotonically at a radius  $r \sim 20\epsilon$ ; this is evidently where softening errors begin to dominate other errors in the force calculation. At the softening radius  $r = \epsilon$ , all three curves show mean acceleration errors  $\delta a/a \simeq 0.013$ .

Are errors of this magnitude dynamically important? In particular, could they explain some of the potential evolution seen in the runs set up with softening (solid curves) in Fig. 11? One possible test is to re-run the simulations using smaller  $\theta$  values; decreasing  $\theta$  from 0.8 to 0.6 or 0.4 reduces the tree code acceleration error associated with softening by factors of  $\sim 2$  or  $\sim 3$ , respectively (albeit at significant computational costs). The new runs were started using exactly the same initial conditions as their  $\theta = 0.8$  counterparts. This initially allows central potentials  $\Phi_{\min}(t)$  to be compared between runs to high accuracy, temporarily circumventing the effects of  $\sqrt{N}$  fluctuations.

Fig. 17 compares Jaffe model results for  $\theta = 0.8$  and 0.4. Initially, the potential difference  $\Phi_{\min}(t; \theta = 0.8) - \Phi_{\min}(t; \theta = 0.4)$  arises because the treecode systematically overestimates the potential well depth by an amount which is greater for larger values of  $\theta$ . As the simulations run, the excess radial acceleration causes systems run with  $\theta = 0.8$  to contract relative to those run with  $\theta = 0.4$ , causing a further increase in potential well depth. This contraction takes place on a dynamical time-scale at  $r \sim \epsilon$ , occurring first for the  $\epsilon = 1/256$  simulations (light grey curves). At later times, as trajectories in otherwise-identical simulations with different  $\theta$  values diverge, short-term fluctuations in  $\Phi_{\min}$  de-correlate and the dispersion in potential differences increases markedly.

These results show that force-calculation errors can have measurable, albeit modest, effects on dynamical evolution. Extrapolating results for a range of  $\theta$  values to  $\theta = 0$ , it appears that for  $\theta = 0.8$  the *dynamical* response of these Jaffe models

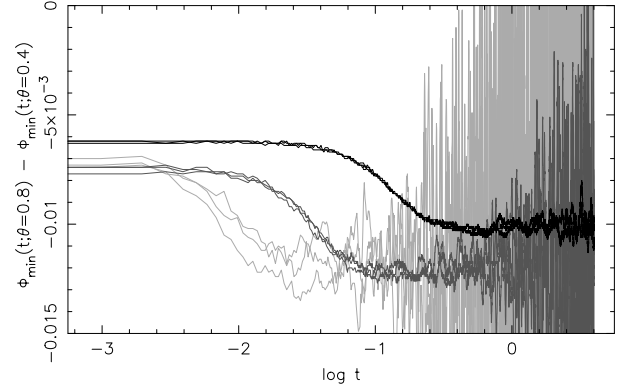


**Figure 17.** Jaffe model results for evolution of difference in potential well depth  $\Phi_{\min}$  for simulations run with  $\theta = 0.8$  and 0.4. Light grey, dark grey, and black show potential differences for  $\epsilon = 1/256$ ,  $1/64$ , and  $1/16$ , respectively; three independent realizations are plotted in each case.

due to excess radial acceleration deepens central potential wells by about 0.2 percent. To test this extrapolation, it would be instructive to repeat these experiments with a direct-summation code. However, compared to the overall range of  $\Phi_{\min}$  variations seen in Fig. 11, the perturbations due to force calculation errors seem relatively insignificant. In addition, density profiles measured from runs with  $\theta = 0.6$  or  $0.4$  appear similar to those shown in Fig. 12, again implying that treecode force calculation errors have little effect on the key results of this study.

The best way to correct (31) for short-range interactions is not obvious. A simple, ad-hoc option is to reduce the effective opening angle on small scales. For example, accepting cells which satisfy

$$d > \frac{\ell}{\theta_{\text{eff}}} + \delta \quad \text{where} \quad \theta_{\text{eff}} = \theta \frac{\epsilon + \ell}{2\epsilon + \ell}, \quad (35)$$

where  $d$  is the distance to the cell's center of mass,  $\ell$  is the cell's size, measured along any edge, and  $\delta$  is the distance between the cell's center of mass and its geometric center (Barnes 1998), reduces softening-relating treecode errors by a factor of  $\sim 2$  at a modest cost in computing time. Further experiments with similar expressions may produce better compromises between speed and accuracy.